Deep-Sea Research I 57 (2010) 1163–1176

Contents lists available at ScienceDirect

Deep-Sea Research I

journal homepage: www.elsevier.com/locate/dsri

Modeled interactions of mesoscale eddies with the East Pacific Rise: Implications for larval dispersal

Diane K. Adams [a,*,1], Glenn R. Flierl [b]

[a] Woods Hole Oceanographic Institution, Woods Hole, MA 02543, USA
[b] Massachusetts Institute of Technology, Cambridge, MA 02139-4307, USA

ARTICLE INFO

Article history:
Received 2 July 2009
Received in revised form
29 May 2010
Accepted 1 June 2010
Available online 19 June 2010

Keywords:
Vortex dynamics
Mesoscale eddies
Hydrothermal vents
Larval dispersal
Ridge topography

ABSTRACT

Larval transport from distant populations is essential for maintenance and renewal of populations in patchy and disturbed ecosystems such as deep-sea hydrothermal vents. We use quasi-geostrophic modeling to consider the potential for long-distance dispersal of hydrothermal vent larvae in mesoscale eddies interacting with the northern East Pacific Rise. Modeled eddy dynamics were similar to the observed propagation dynamics of Tehuantepec eddies, including their ability to cross the ridge. Simulated surface anticyclones were associated with coherent cyclones in the deep layer with relatively strong current velocities that could significantly increase the dispersal potential of passive particles. Eddy interactions with ridge topography further enhanced tracer dispersal along the ridge axis through shearing and elongation of the eddy core. Simulations suggest that the passage of an eddy would result in local loss from the vent field and aggregate transport with potential enhancement of dispersal between vent fields separated by up to 270 km. Based on the latitude at which most Tehuantepec eddies cross the ridge, eddy-induced flows would enhance connectivity between the 13°N, 11°N, and 9°N vent fields along the East Pacific Rise asymmetrically with higher transport from northern vent fields to southern vent fields.

Published by Elsevier Ltd.

1. Introduction

Dispersal in mesoscale eddies has been shown to contribute to the connectivity of benthic populations with patchy distributions (e.g. reef and island fauna, Boehlert et al., 1992; Lee et al., 1994; Nakata et al., 2000; Sale, 1970). Eddies can propagate for weeks to months (Goni et al., 1997; Palacios and Bograd, 2005; Sangrá et al., 2005) potentially transporting water and associated larvae 100s–1000s of kilometers between populations. During this transport, high productivity induced by upwelling (Backus et al., 1981) and residual 'island mass effects' (Doty and Oguri, 1965; Heywood et al., 1996) in some eddies may enhance the growth and survival of larvae (Emery, 1972; Nakata et al., 2000). Since the larvae would be transported as a group within the eddy core, high numbers of larvae can be delivered in pulses as an eddy passes suitable recruitment sites (Sponaugle et al., 2005).

If eddies observed at the surface extend into the deep sea, they have the potential to effect dispersal between deep benthic populations in patchy habitats such as hydrothermal vents. Mesoscale eddies interact with portions of the mid-ocean ridge globally (e.g. Walvis Ridge and Mid-Atlantic Ridge, Goni et al., 1997; Schonten et al., 2000; Southeast Indian Ridge, de Ruijter et al., 2004; East Pacific Rise, Palacios and Bograd, 2005). Most eddies propagate to the west due to the latitudinal variation in the Coriolis parameter, called the β–effect (Cushman-Roisin et al., 1990; Nof, 1981). Since hydrothermal vents are primarily aligned north–south along a ridge axis (e.g. Juan de Fuca, East Pacific Rise, Mid-Atlantic Ridge), transport between vents due to mean eddy propagation seems unlikely. However, the clockwise or counter-clockwise rotation, hereafter referred to as the swirl, of an eddy could transport larvae between vent sites if the eddy encompasses two or more vent fields. Although, swirl velocities are generally considered to be relatively weak at depth (Mulhearn et al., 1986; Richardson and Fratantoni, 1999; Tracey et al., 2006) (order 10 cm s^{-1} at 4000 m compared to 100 cm s^{-1} at the surface), deep eddy-induced currents could be significant compared to the slow background current velocities, less than 10 cm s^{-1}.

Multiple eddies generated by wind jets (Ballestero and Coen, 2004; McCreary et al., 1989; Müller-Karger and Fuentes-Yaco, 2000) and baroclinic instabilities (Ballestero and Coen, 2004; Farrar and Weller, 2006; Hansen and Maul, 1991; Zamudio et al., 2006) in the Gulfs of Tehuantepec and Papagayo, off the coast of Central America (Fig. 1), propagate westward across the East Pacific Rise each year (Palacios and Bograd, 2005). Tehuantepec

* Corresponding author. Tel.: +1 301 496 1392; fax: +1 301 480 5353.
E-mail addresses: dadams@whoi.edu (D.K. Adams), glenn@lake.mit.edu (G.R. Flierl).
[1] Present address: National Institutes of Health, National Institute of Dental and Craniofacial Research, 30 Convent Drive, Bethesda, MD 20892, USA.

0967-0637/$ - see front matter Published by Elsevier Ltd.
doi:10.1016/j.dsr.2010.06.009

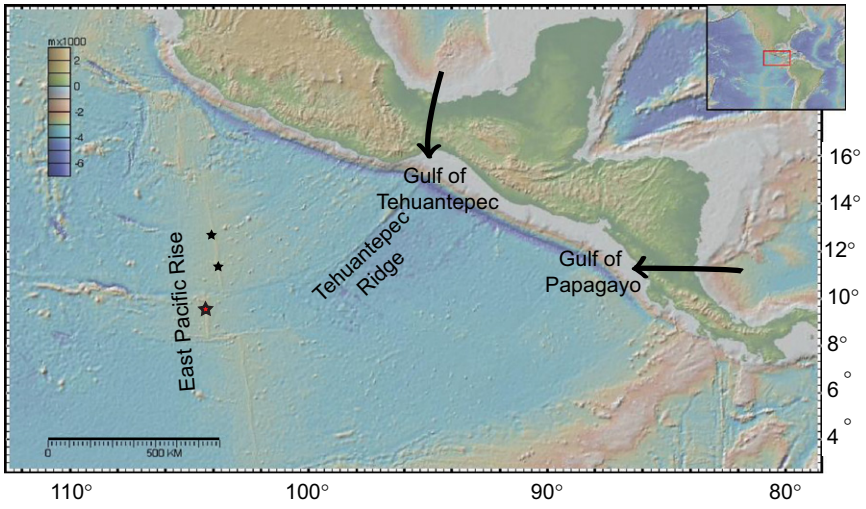

Fig. 1. Topography of Central America and bathymetry of the East Pacific. Arrows indicate the location of two mountain-pass wind jets near the Gulfs of Tehuantepec and Papagayo. Wind jets are formed when high pressure develops over the Gulf of Mexico causing air to flow rapidly through the passes down the pressure gradient. The bathymetry shows the Tehuantepec Ridge and East Pacific Rise. The 9°N, 11°N and 13°N vent fields are noted as stars. Map created in GeoMapApp.

and Papagayo eddies often reach diameters of 100–450 km at the surface. If the extent of the eddies were similar at depth, the size would be sufficient to encompass multiple vent fields along the East Pacific Rise.

The main goal of this study was to investigate the potential for mesoscale eddies to influence the near bottom transport of hydrothermal vent larvae. We specifically consider the interaction between anticyclonic mesoscale eddies resembling Tehuantepec eddies and the East Pacific Rise. Since Palacios and Bograd (2005) observed that Papagayo eddies, between 1992 and 2004, always dissipated or merged before crossing the East Pacific Rise, we focused on interactions of Tehuantepec eddies with the ridge and their potential to transport vent larvae. We use a two layer quasi-geostrophic model of an isolated vortex to investigate the flow in the deep layer and potential for larval transport in these flows. To verify that the model is consistent with observations of Tehuantepec eddies, we analyzed the general dynamics of the modeled eddies in the surface and at depth with a flat bottom and with averaged East Pacific Rise topography. We then introduced a tracer, with and without settlement behavior, into the bottom layer of the model to investigate the potential for larval transport along the ridge.

2. Methods

2.1. Quasi-geostrophic model

A rigid-lid, two-layer quasi-geostrophic model was employed to investigate the effects of an isolated vortex on the currents and transport in the deep sea. The quasi-geostrophic approximation assumes that the dominant forces, the Coriolis force and the pressure gradient force, are in geostrophic balance but accounts for ageostrophic corrections such as the inclusion of topographic effects and nonlinear forces associated with the rotation of the vortex. Based on these assumptions, the dimensional quasi-geostrophic equations for two layers were used in the following form (as in Pedlosky, 1996, Eqs. (3.2.34) and (3.2.36)),

$$q_1 = \nabla^2\psi_1 + F_1(\psi_2 - \psi_1) + \beta y$$

and

$$q_2 = \nabla^2\psi_2 + F_2(\psi_1 - \psi_2) + \beta y + \frac{f_0}{H_2}b$$

for

$$F_i = \frac{f_0^2}{g' H_i},$$

where q_i is the potential vorticity and ψ_i is the stream function in each layer ($i=1$ and 2, surface and deep layers, respectively); f_0 is the Coriolis parameter at the center of the domain, β is the northward gradient of the Coriolis parameter, and y is the meridional (north–south) distance from the center of the domain; b is the topographic elevation; H_i is the mean depth of layer i, and g' is the reduced gravity. When the flow is geostrophic, ψ is related to pressure as $\psi = p'/(\rho_0 f_0)$, where p' is the pressure and ρ_0 is the density. The reduced gravity was not an explicit parameter, but was calculated based on the Rossby radius of deformation, R_D, and the relationship $F_1 + F_2 = 1/R_D^2$.

From these equations, the zonal (east-west, u_i) and meridional (v_i) components of the velocity in each layer are given by

$$(u_i, v_i) = \left(-\frac{\partial}{\partial y}\psi_i, \frac{\partial}{\partial x}\psi_i\right).$$

The stream function thus gives the direction (along the contours) and the speed (inverse to the spacing between contours) of flow. The potential vorticities are conserved following the geostrophic flow

$$\frac{\partial q_i}{\partial t} + u_i\frac{\partial q_i}{\partial x} + v_i\frac{\partial q_i}{\partial y} = 0.$$

Our two layer model was built on the Fortran-77 pseudospectral code of Dewar (1983), but has been substantially modified (e.g., Flierl, 1994). Friction was not explicitly modeled and no bottom friction was included, but an exponential wavenumber cutoff filter (Canuto et al., 1988) was employed to dampen variability at small spatial scales, similar to the effects of frictional viscosity. The vortices were modeled on a 1536 km × 1536 km domain, with periodic boundary conditions and a 3 km grid size.

The range of model parameters was set as follows to generally represent observations of Tehuantepec eddies from

Table 1
Characteristics of anticyclonic Tehuantepec eddies from published literature.

Propagation		Radius (km)	Swirl ($cm\,s^{-1}$)	Data source	Ref.
Direction	Speed ($cm\,s^{-1}$)				
Tehuantepec					
258°	9–21 (16)	120	–	SST, Color	Müller-Karger and Fuentes-Yaco (2000)
–	8.5	150	80	Model	McCreary et al. (1989)
–	–	50-200	–	SLA	Palacios and Bograd (2005)
–	4.7–8	85–200	–	SST, Color	Gonzalez-Silvera et al. (2004)
–	16.7	200	–	SLA, DH	Giese et al. (1994)
–	14.6	168	–	Drifters, CTD, SLA	Hansen and Maul (1991)
–	–	100–160	50–100	Model	Zamudio et al. (2006)
243–257°	8–11	90–175	65	SLA	Adams (2007)
–	11–19	90–250	>100	Review	Willett et al. (2006)

Propagation direction is degrees from north. SST: sea surface temperature; Color: ocean color; SLA: sea level anomaly from altimetry; DH: dynamic height. Note that the radius for most cases may be the total radius, not the *e*-folding radius.

the literature (Table 1),

$H_1 = 547\,\text{m}, \quad H_2 = 2733\,\text{m},$

$f_0 = 2.48 \times 10^{-5}\,\text{s}^{-1}, \quad \beta = 2.20 \times 10^{-8}\,\text{km}^{-1}\,\text{s}^{-1},$

$R_D = 90\,\text{km}, \quad l = 50-200\,\text{km},$

$V_1 = -150-50\,\text{cm}\,\text{s}^{-1},$

where f_0 is the Coriolis parameter at 9°50′N and l is the *e*-folding radius. R_D=90 km was chosen for this study to represent conditions near the hydrothermal vents at 10°N (Chelton et al., 1998). The qualitative results were not sensitive to the small difference in R_D between the Gulf of Tehuantepec and the 10°N hydrothermal vents, R_D=70 and 90 km, respectively (Chelton et al., 1998) (data not shown). Eddies were initiated with a Gaussian shape with an initial swirl speed, V_i, in each layer i, where $V_i<0$ is anticyclonic and $V_i>0$ is cyclonic. These parameters represent strongly baroclinic and moderately nonlinear anticyclonic eddies similar to observations and previous modeling of eddies in the eastern tropical Pacific (e.g., Gonzalez-Silvera et al., 2004; McCreary et al., 1989; Müller-Karger and Fuentes-Yaco, 2000) (Table 1).

Based on the initialization parameters tested (Appendix A), a set of standard parameters was used throughout the experiments unless otherwise noted; viz.,

$l = 100\,\text{km}, \quad V_1 = -75\,\text{cm}\,\text{s}^{-1}, \quad V_2 = 15\,\text{cm}\,\text{s}^{-1}.$

The lower layer swirl speed was chosen to decrease the radiation of Rossby waves in the lower layer (see Appendix A.1). A background flow of u_1=5 $cm\,s^{-1}$ to the west was included in the upper layer to mimic the regional mean flow (Fiedler and Talley, 2006); no background flow was included in the lower layer. Results were not sensitive to the inclusion of background flow in either layer (data not shown).

Fluid transport in the lower layer was visualized by including a Gaussian tracer patch with radius $\frac{3}{4}$ / centered at the initial eddy position. The tracer was passively advected by the simulated lower layer flows, V_2. Diffusion was not explicitly incorporated, but numerical diffusion contributed to the spread of the tracer.

Willett et al. (2006) suggested that the tropical Pacific eddies are more like frontal-geostrophic eddies than quasi-geostrophic eddies because the eddies are nonlinear enough that the displacements of the pycnocline are not very small compared to the mean thickness of the pycnocline, 500–600 m (Fiedler and Talley, 2006). However, the l:R_D ratio rarely met the frontal-geostrophic requirement that $l>3R_D$ (Table 1). More importantly here, the frontal-geostrophic approximation assumes an infinitely deep lower layer, making it inappropriate for questions about flow in the lower layer and interactions with topography. Chassignet and Cushman-Roisin (1991) demonstrated the importance of the lower layer; their results, in comparison with McWilliams and Flierl (1979), suggest that the quasi-geostrophic approximation should give a reasonable representation of the flow.

2.2. Ridge topography

Changes in the deep layer flows and surface propagation were investigated with the inclusion of ridge topography. Ridge topography was modeled from real cross-sections of the 9°N segment of the East Pacific Rise. Topographic data from fifteen 256 km wide, zonal cross-sections of the EPR obtained using GeoMapApp (Carbotte et al., 2004) were averaged. Cross-sections were not taken through lines intersecting seamounts. The mean ridge cross-section was projected meridionally in the model domain. Transform faults, lower-order breaks in ridge topography, and the axial summit trough were not included. The 1536 km × 1536 km domain consisted of a flat bottom with depth H, where $H = H_1 + H_2$, latitudinally centered at 9°50′N. For ridge experiments the eastern edge of the ridge topography was positioned at the domain center such that the ridge axis (maximum elevation) was located 130 km to the west of the domain center. Simulations were run for the reference flat-bottom case (without topography) and with the ridge topography to assess the effect of the ridge on eddy propagation and deep-layer currents.

2.3. Larval transport and settlement

The potential impact of eddy-induced currents on larval transport was considered by introducing small patches of tracer at various positions along the longitude of the ridge axis. The patches conceptually mimicked production at the 9°N, 11°N, and 13°N vent fields. Tracer patches with a Gaussian-distribution and an e-folding radius of 10 km were used due to resolution constraints. The spread of the tracer patch along the position of the ridge axis was recorded over time as an eddy passed over the ridge. Tracer concentrations were plotted relative to the initial source maximum.

Settlement behavior was modeled as

$$\frac{\partial}{\partial t}b + u_i\frac{\partial}{\partial x}b + v_i\frac{\partial}{\partial y}b = -sb,$$

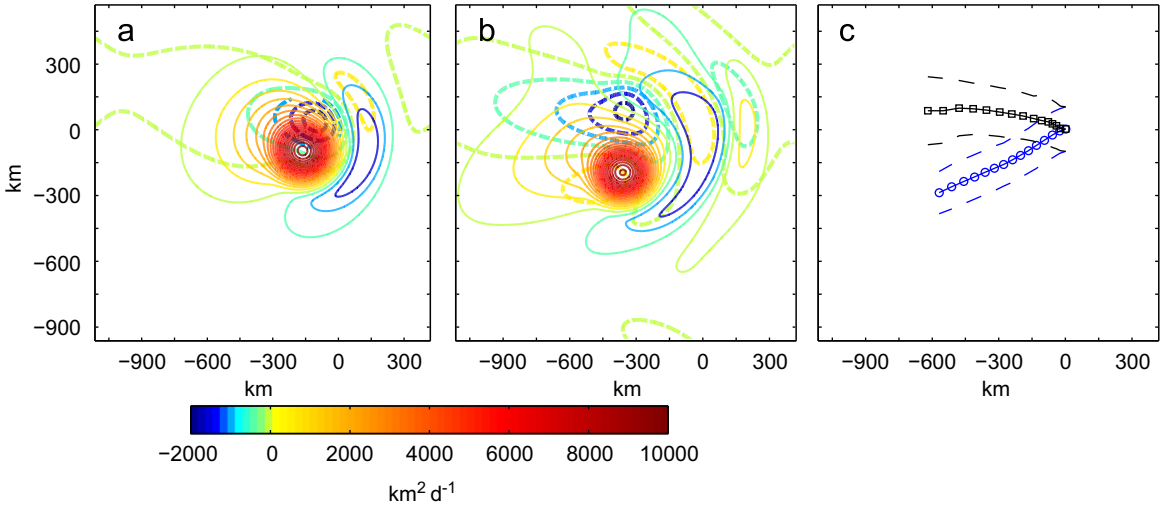

Fig. 2. Contours of the stream function at (a) day 25 and (b) day 50 in the upper (solid contour lines, warm tones) and lower (dashed contour lines, cool tones) layers using standard parameters. The contour interval was 500 $km^2\,d^{-1}$ for both plots. (c) Differences in propagation were also visible in the trajectories of the spatial maximum of ψ_1 in the upper layer (blue lines, circles) compared to the spatial minimum of ψ_2 in the lower layer (black lines, squares) over 70 days. Dashed lines denote the size of the eddy as measured by distance from the spatial maximum/minimum of ψ_i to the maximum velocity. Symbols indicate positions every $\Delta t = 5.0$ d. The origin is placed at the initial position of the eddy. (For interpretation of the references to colour in this figure legend, the reader is referred to the web version of this article.)

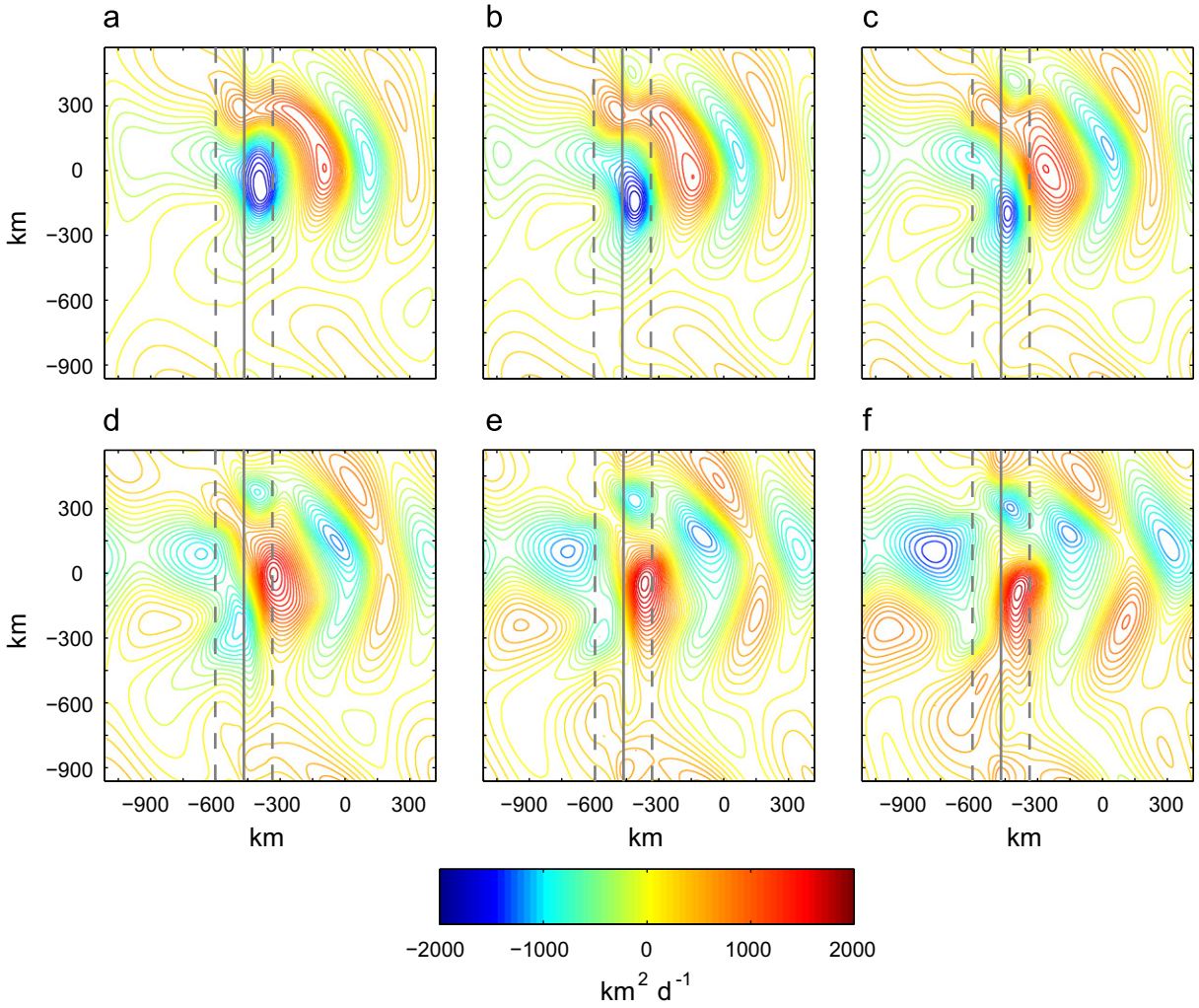

Fig. 3. Plan views of the stream function in the lower layer, ψ_2, showing the evolution of the cyclone (dark blue) with standard parameters as it crosses ridge topography. Anticyclones and cyclones develop to the east in the eddy wake. The contour interval was 100 $km^2\,d^{-1}$ for all plots. The solid gray line denotes the ridge axis. The dashed gray lines denote the extent of the topography. The origin is placed at the initial position of the eddy. In this and subsequent figures, the fields are plotted at five day intervals from day 50 to day 75. (a) t=50 d. (b) t=55 d. (c) t=60 d. (d) t=65 d. (e) t=70 d. (f) t=75 d.

where

$$s = \begin{cases} s_0 e^{(-0.5(x-x_0)^2)/W^2} \left(\dfrac{t-20}{t-20+t_{1/2}}\right) & \text{for } t \geq 20\,\text{d}, \\ 0 & \text{for } t < 20\,\text{d}. \end{cases}$$

W is the zonal e-folding radius, $t_{1/2}$ is the time at which half of the maximum settlement rate is reached (roughly equivalent to an average precompetency period), s_0 is the maximum settling rate, and x_0 is location of the ridge axis. The 20 day delay in settlement was included to prevent settlement of the tracer before the influence of the eddy reached the ridge. Experiments were run with $W = 1$ km, $s_0 = 0.5\,\text{d}^{-1}$ and $t_{1/2} = 5$ d to represent relatively smart larvae that settle when in close proximity to the ridge axis, x_0. A short $t_{1/2}$ was chosen because the larval pool would likely contain a mixture of ages, with some initially competent to settle; and the precompetency period for many lecithotrophic larvae may be on the order of a few days.

Maximum transport distances were estimated for the passive tracer transport experiments and the settlement experiments, based on an estimate of 100,000 larvae km^{-2} as the initial maximum concentration (assuming 100 larvae per 40 m^3 (Mullineaux et al., 2005) and a vent field 40 m in width and 1 km in length). Due to resolution constraints and the grid size, we conservatively defined the maximum extent of transport where the tracer concentration or cumulative settlement reached 1/1000th the initial maximum concentration (100 larvae $\text{km}^{-2}\,\text{d}^{-1}$ or 100 larvae km^{-2} over a given time, respectively).

3. Results

3.1. Currents at depth

In all the experiments, a cyclonic eddy in the deep layer accompanies the surface anticyclone (Fig. 2). Development of a cyclone was independent of the initial swirl speed or direction. (Details of the experiments varying initialization conditions in the deep layer can be found in Appendix A.) The deep cyclone propagated in association with the surface anticyclone as a cohesive geostrophic feature with current velocities sufficiently strong to transport tracer within its core.

3.2. Topographic effects

While the ridge topography had small effects on the surface anticyclone (see Appendix B), it had a more substantial effect on the cyclonic eddy in the lower layer (Fig. 3) when compared to the flat bottom case (Fig. 4). The cyclone elongated along the ridge and deflected towards the south upon initial contact with ridge topography (Fig. 3a–c). The eastern ridge flank compressed the

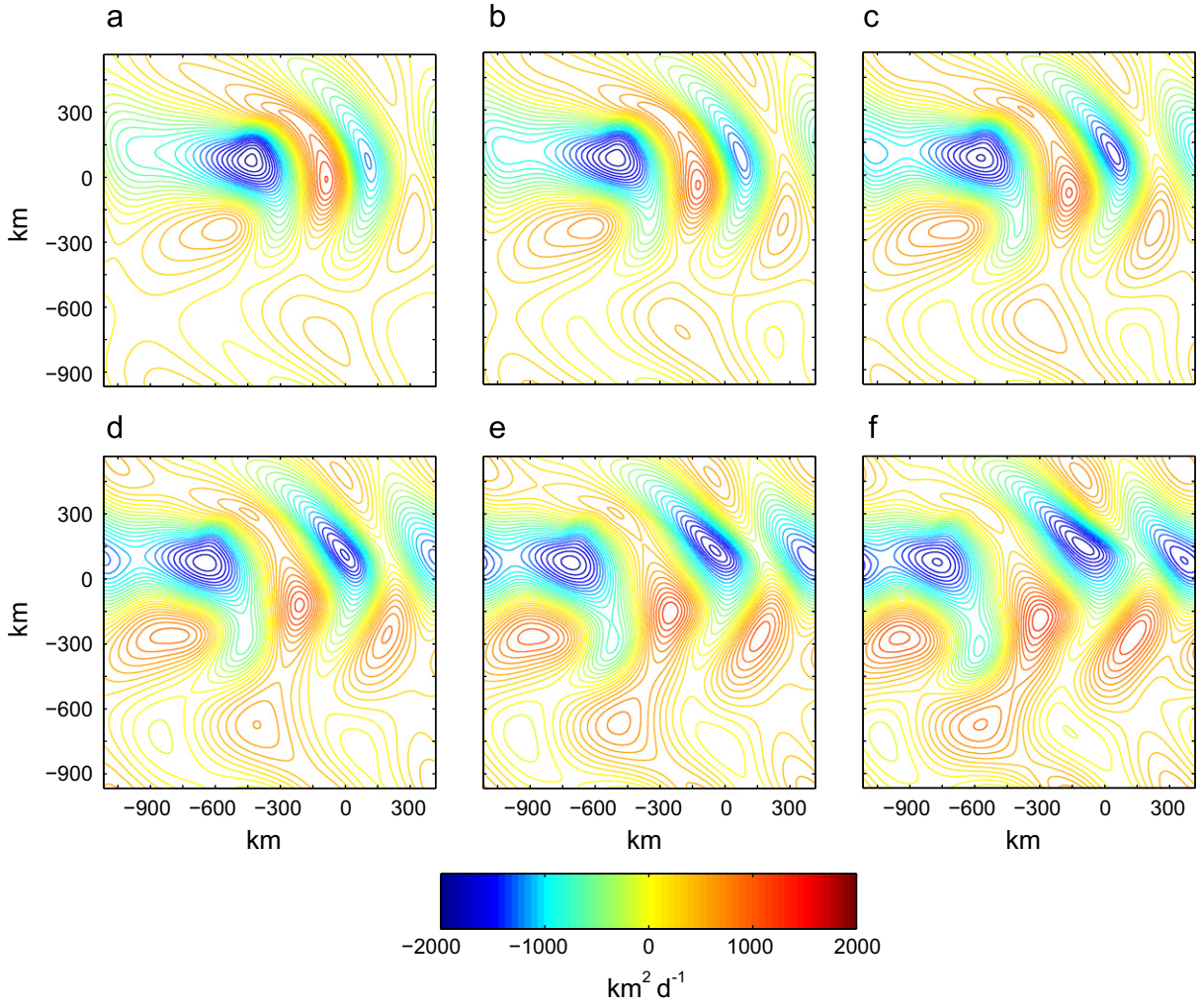

Fig. 4. As in Fig. 3, but for the flat bottom case. The contours remained similar to the case with topography for the first 30 days. (a) $t=50$ d. (b) $t=55$ d. (c) $t=60$ d. (d) $t=65$ d. (e) $t=70$ d. (f) $t=75$ d.

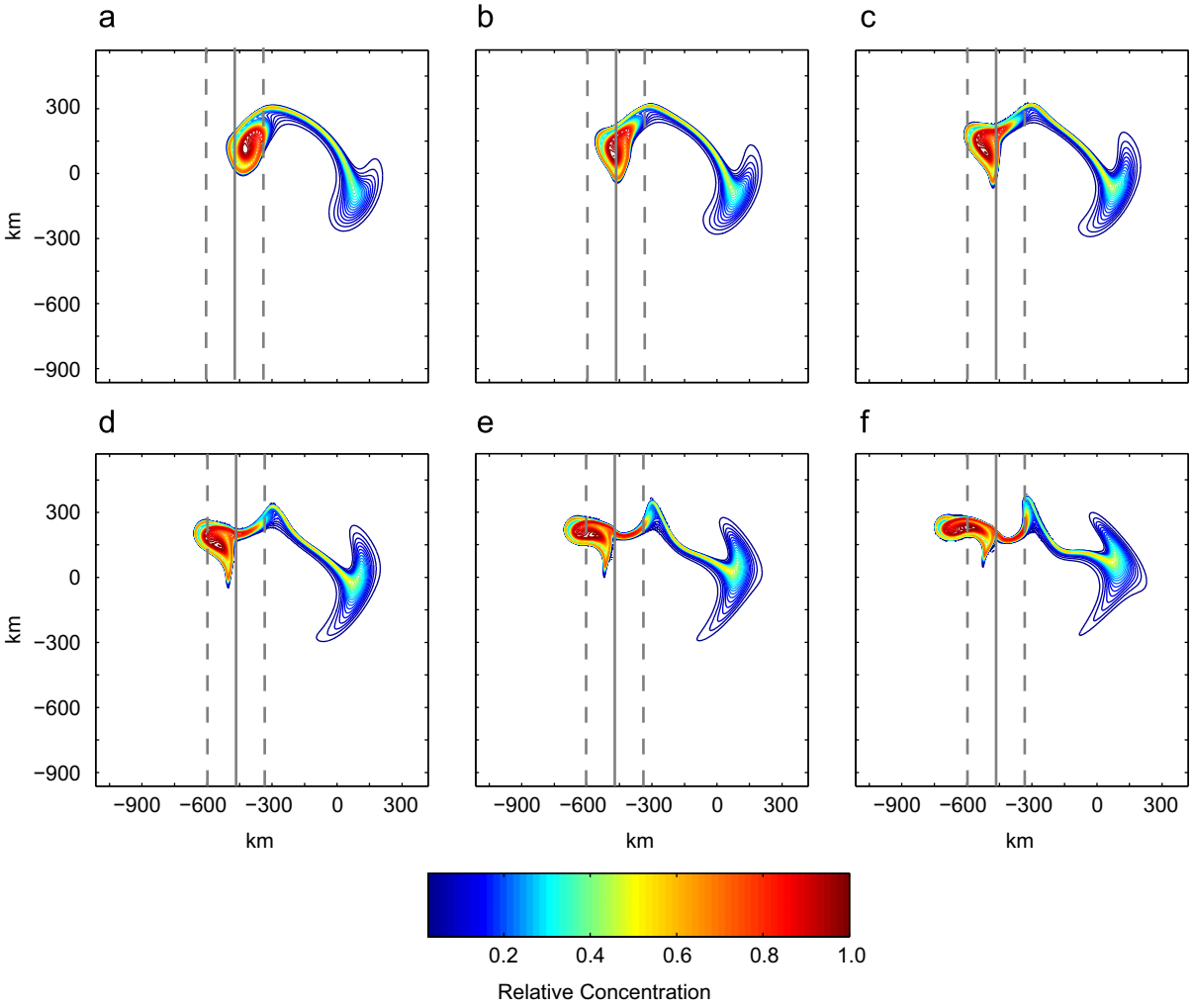

Fig. 5. Plan views of the concentration of tracer (normalized to the initial maximum) in the lower layer showing the transport of water in the cyclone core as it crosses the ridge. Some tracer was not transported within the cyclone, leaving a trail of tracer with low concentration (cool colors) compared to the tracer within the core (warm colors). The contour interval is 0.025 for all plots. The solid gray line denotes the ridge axis. The dashed gray lines denote the extent of the topography. The origin is placed at the initial position of the eddy. (a) $t=50$ d. (b) $t=55$ d. (c) $t=60$ d. (d) $t=65$ d. (e) $t=70$ d. (f) $t=75$ d. (For interpretation of the references to colour in this figure legend, the reader is referred to the web version of this article.)

fluid adding anticyclonic vorticity. This ridge-induced anticyclonic vorticity weakened the cyclone (decreased range of ψ associated with the cyclone) and later strengthened the trailing anticyclone. However, the compression and elongation also induced strong north–south currents, reaching up to a maximum v_2 of 27.6 cm s^{-1}, and a maximum v_2 of 23.3 cm s^{-1} on the ridge axis (as seen in the close spacing of contour lines in Fig. 3a–c). Contours of the stream function showed the propagation of the northern half of the cyclone over the ridge (Fig. 3c, d). Once over the ridge axis, the decrease in elevation added cyclonic vorticity, strengthening the cyclone and 'pulling' the southern portion across the ridge (Fig. 3d–f).

Tracer experiments indicated that the core of the cyclone deformed as it interacted with the topography but did not split (Fig. 5). Tracer was transported over the ridge in a coherent mass with deformation from zonal compression and meridional elongation induced by the ridge topography. The tracer trajectory only transiently deviated from the reference tracer trajectory in the flat bottom case (Fig. 6), suggesting that the elongated water mass along the ridge to the south of the eddy center was likely from outside of the eddy core.

3.3. Tracer transport and settlement

Larval dispersal potential was assessed by advecting tracer patches placed at various locations along the location of the ridge axis, with a flat-bottom (Figs. 7a and 8a) and with ridge topography (Figs. 7b and 8b), for an eddy with standard parameters. Tracer was allowed to settle when in close proximity to the ridge. Maximum transport distances were not significantly different between the passive tracer and the settled tracer, suggesting that the maximum dispersal distance was not sensitive to changes in the abundance of tracer. Tracer patches were initially positioned on the ridge axis 100 km to the north of, at the center of, and 100 km to south of the center of the eddy when it crossed the position of the ridge axis. For all cases, with and without topography, the eddy-induced currents initially displaced the tracer from the starting location, resulting in local loss of tracer. Return of tracer to the initial longitudinal position (ridge axis) varied based on the initial position relative to the path of the cyclone. Thus, the settlement was sensitive to the vertical structure and initial position of the eddy in this model, since it depends on the latitude of the deep eddy when it crosses the ridge

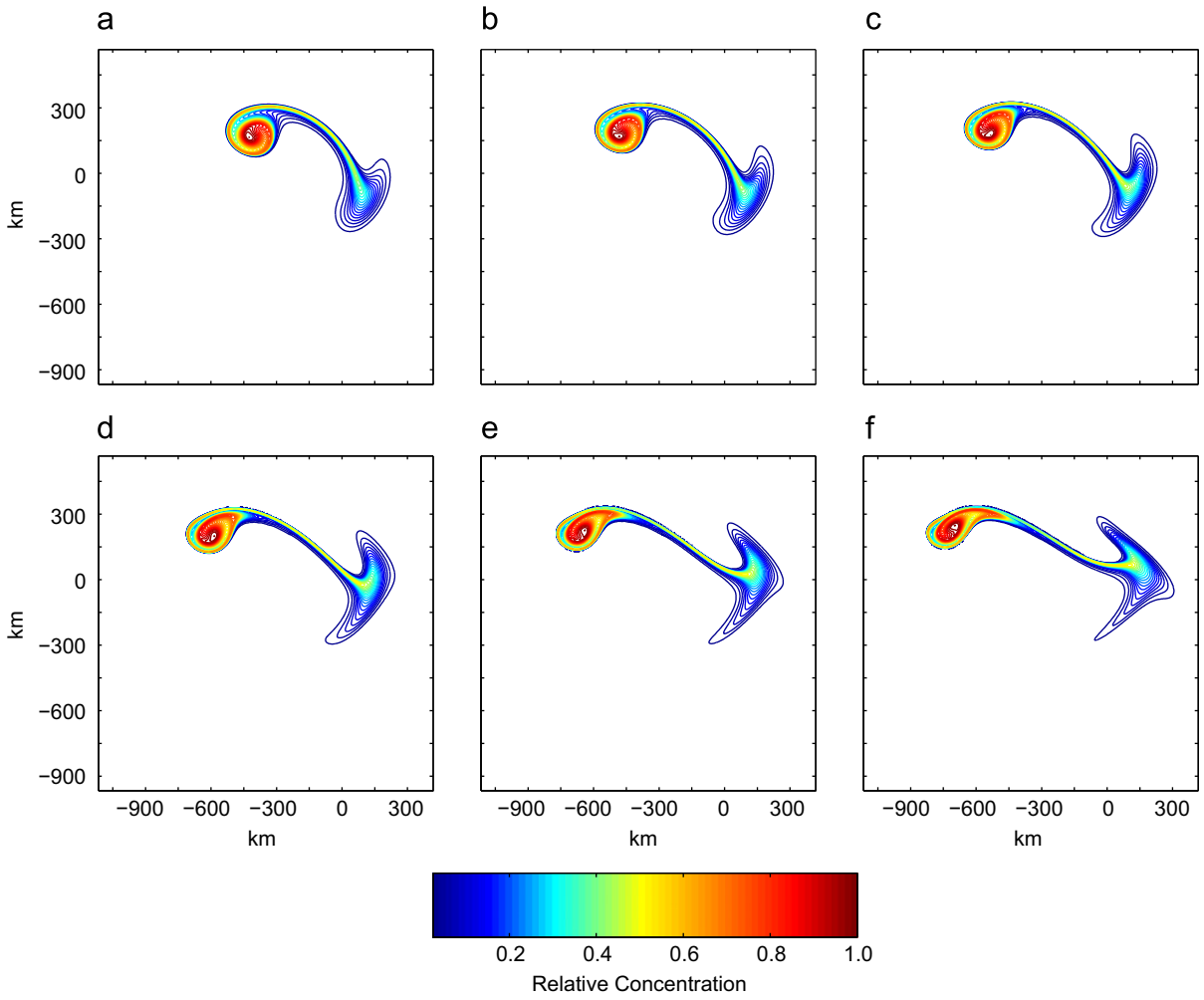

Fig. 6. As in Fig. 5, but for the flat bottom case. The contours remained similar to the case with topography for the first 30 days. (a) $t=50$ d. (b) $t=55$ d. (c) $t=60$ d. (d) $t=65$ d. (e) $t=70$ d. (f) $t=75$ d.

compared to the latitude of the source. We present experiments with standard parameters (detailed below) which illustrate typical variation in settlement by factors of two or more, and demonstrate our main point that the deep eddy flows as influenced by the topography are quite capable of spreading larvae along the ridge.

For the flat-bottom case, tracer returned to the ridge axis only for the patch initiated 100 km to the north (Fig. 7a). A maximum of 45% of the initial concentration returned to the original longitudinal position at day ~60 (Fig. 7a, top panel).

Ridge topography enhanced meridional tracer transport and enhanced return to the ridge axis through elongation and shearing of the tracer patches (Fig. 8b compared to the flat bottom case Fig. 8a). The northern patch was advected westward and sheared to the north resulting in the eastward return of a thin filament to the ridge axis a maximum of 150 km to the north of the initial position at 60 days. This filament contributed to a settlement peak centered 99 km to the north of the starting position, with larval concentrations reaching over 20% of the initial maximum (Fig. 9b). The leading edge of the filament was then advected westward back onto the ridge on day ~90, reaching 170 km north of the starting position. Southward transport from the northern patch was not enhanced by eddy-induced currents.

Southward transport was greatly enhanced by eddy-induced currents for the patch initiated at the center of the eddy path. The center tracer patch was initially advected south-southwest. Elongation of the patch kept a portion of the tracer patch on the ridge axis throughout the experiment, resulting in the highest total fraction settled (Fig. 9a) and high settlement away from the starting position; a secondary peak in settlement of 83% of the initial concentration occurred 108 km south of the starting position on approximately day 85 (Fig. 9c). The tracer reached a maximum southern displacement of 270 km on day 66 (Fig. 7b, center panel). Transport from the center patch to the north was not enhanced by eddy-induced currents.

Transport from the patch initiated 100 km south of the center of the eddy path was not greatly enhanced by eddy-induced currents in either direction (Fig. 7b, lower panel, and Fig. 9d). Tracer was initially deflected to the south but quick transport off axis and less shearing in the periphery of the eddy core prevented enhanced southward transport. Tracer was quickly advected to the north then west and brought back towards the ridge; however, the tracer did not return all the way to the ridge axis (Fig. 8b, bottom panel). Under other conditions (e.g. a lower ridge or a stronger eddy), the southern tracer patch did return to the ridge axis and eddy-induced currents enhanced transport up to 150 km to the north (data not shown).

4. Discussion

Our results indicate that mesoscale eddies have the potential to significantly impact the dispersal of larvae along the East

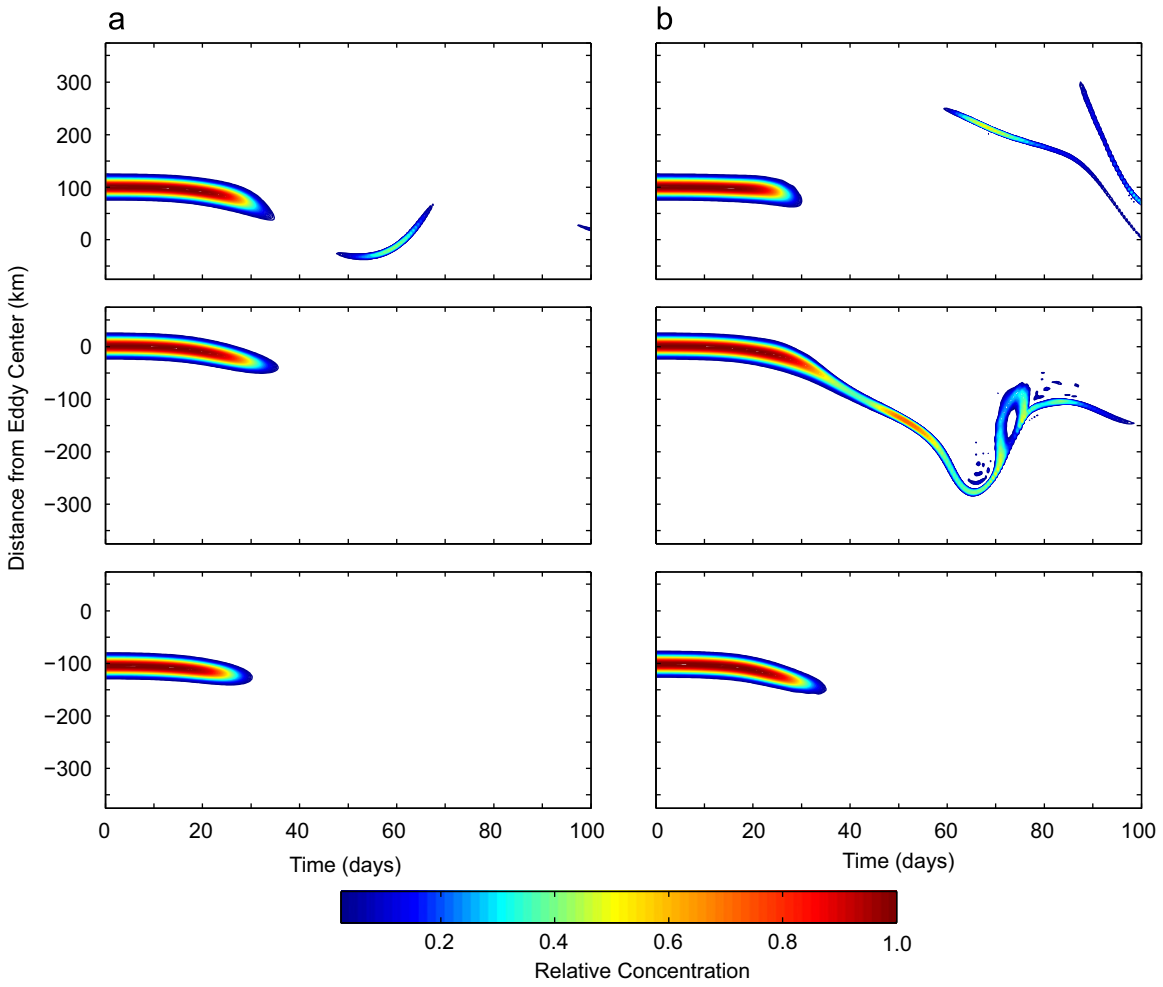

Fig. 7. Time-series of the concentration of tracer, relative to the initial maximum, (a) on a flat bottom and (b) on ridge topography for tracer patches starting along the zonal position of the ridge axis and placed meridionally 100 km north of the center of the eddy path (top), at the center of the eddy path (center), and 100 km south of the center of the eddy path (bottom) for an eddy with standard parameters. The origin is placed where the center of the eddy crosses the position of the ridge axis. The contour interval is 0.01 for all plots. (a) Flat bottom. (b) Ridge topography.

Pacific Rise (EPR). The influence of the simulated mesoscale eddies extended into the deep layer with the potential to induce currents exceeding 20 cm s^{-1} on the ridge axis, twice the speed of 'typical' currents (Adams and Mullineaux, 2008; Chevaldonné et al., 1997; Kim et al., 1994; Marsh et al., 2001). These strong currents could significantly increase the potential dispersal distance of a larva. If larvae act as passive particles, the tracer results can be applied to gain insight into larval dispersal. Interactions with ridge topography enhanced tracer dispersal along the ridge axis through shearing and elongation of the eddy core. Simulations suggest that the end result of an eddy passing would be local loss of larvae from the ridge axis and aggregate transport of larvae with potential enhancement of dispersal between vent fields. During the passage of an eddy, tracer (larval) concentrations were advected in eddy-induced currents up and down the ridge, sometimes distances greater than 150 km (the approximate distance between vent fields along the northern EPR). Larger eddies have the potential to advect passive particles, including larvae, even greater distances.

4.1. Applicability to Tehuantepec eddies

The propagation characteristics of simulated eddies were similar to surface observations of Tehuantepec eddies. Modeled propagation speeds (see Appendix A.2) were within the range of observations in the literature (Table 1). The simulated trajectories were generally oriented more to the south compared to observations, but by less than a 5° difference in direction. Interactions with the Tehuantepec Ridge (Fig. 1) may account for this minor discrepancy in the direction of propagation. Interactions with the East Pacific Rise and the Clipperton fracture zone, running zonally between 10°10′N and 10°20′N, may also steer eddy trajectories slightly more northerly. Still, the model captured general propagation dynamics of the surface eddy quite well, even without the inclusion of the Clipperton fracture zone and the Tehuantepec Ridge. This suggests that while the seafloor bathymetry may help to steer surface eddy propagation and could have a larger effect on the deep currents, the effects on surface eddy propagation are minimal.

4.2. Eddies reach the deep sea

The importance of Tehuantepec eddies and mesoscale eddies, in general, in the euphotic zone has been well studied, but the deeper influence of eddies has been largely ignored. We showed that simulated anticyclonic mesoscale eddies were accompanied by coherent cyclones in the deep layer. Eddies initialized with the standard parameters developed current velocities in the deep layer often exceeding 25 cm s^{-1}. While these velocities were

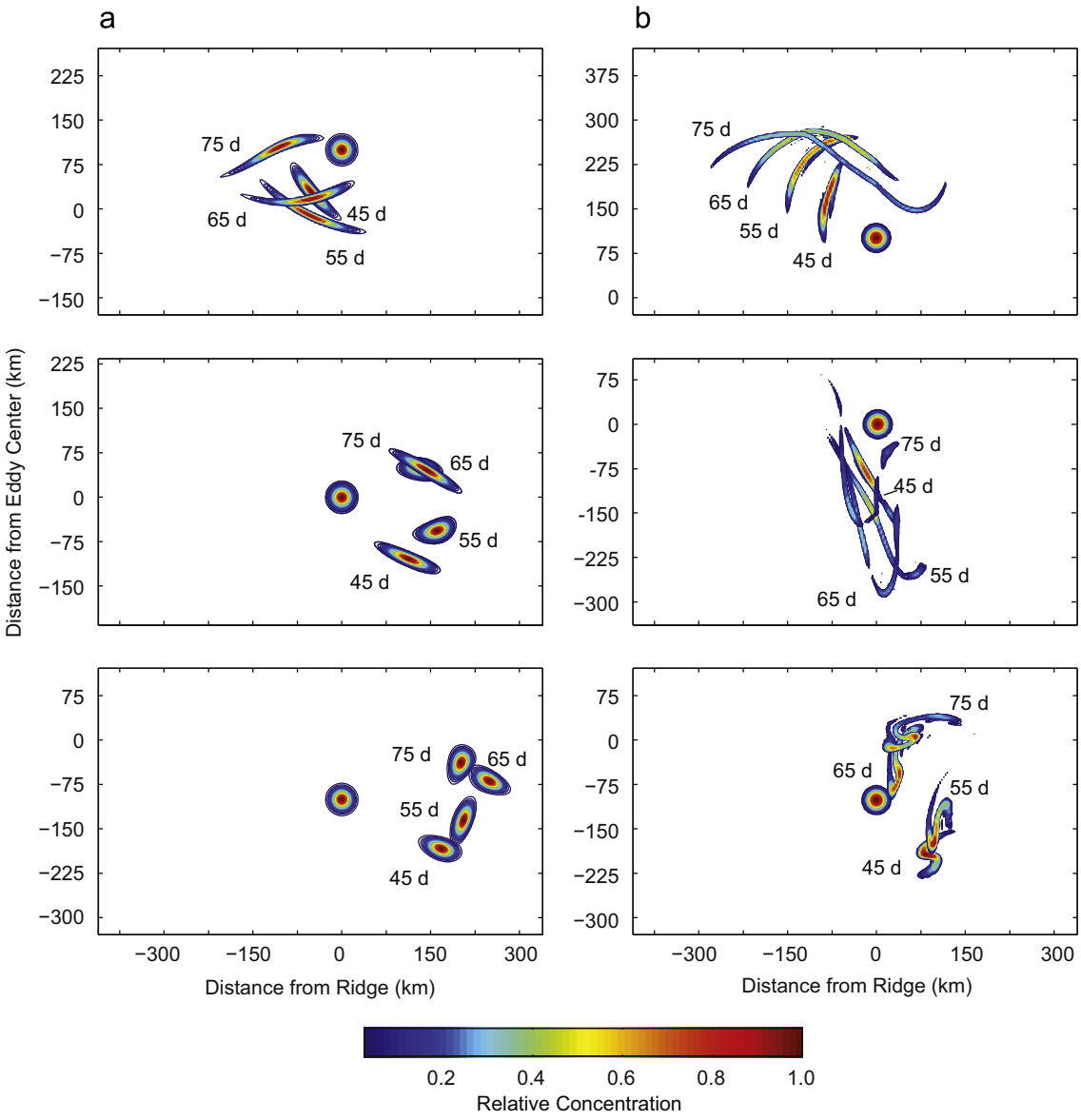

Fig. 8. Spatial distribution of tracer patches over (a) flat bottom and (b) ridge topography at their initial position and every 10 days from day 45 to day 75. Tracer patches had starting positions at the zonal position of the ridge axis and were positioned meridionally 100 km to the north of the center of the eddy path (top), at the center of the eddy path (center), and 100 km to the south of the center of the eddy path (bottom). The eddy was modeled using standard parameters. The origin is placed where the center of the eddy crosses the position of the ridge axis. The contour interval is 0.025 for all plots. (a) Flat bottom. (b) Ridge topography.

small compared to the velocities within the surface anticyclone, in the deep sea, these velocities represent a significant increase in fluid flow and energy. Furthermore, the modeled cyclonic eddy was a coherent structure able to carry a patch of tracer within its core with minimal loss. These observations suggest that the influence of the surface eddy at depth could have a significant impact on the transport of material in the deep sea, including falling marine snow and deep-sea larvae, in general.

The presence of a vertical dipole in our simulated eddies is surprising in the context of ring observations (Clement and Gordon, 1995; Mulhearn et al., 1986; van Aken et al., 2003), but is consistent with geophysical fluid dynamic theory. Flierl et al. (1983) and Flierl (1987) proposed the 'no net angular momentum theory' in which a slowly varying, isolated disturbance on the beta plane must have zero net relative angular momentum to satisfy

$$\beta \int \int \psi = 0.$$

In other words, an isolated eddy must be, by definition, self-contained—have no net angular momentum. The simplest way to achieve this is via a dipole, so that the angular momentum of the anticyclone and cyclone counterbalance each other. Although the theory was initially applied to horizontal barotropic dipoles (surface anticyclonic and cyclonic eddies pairs next to each other), vertical dipoles like the ones modeled here also satisfy the condition for baroclinic vortices.

Numerical modeling studies (Hyun and Hogan, 2008; Zamudio et al., 2006) and an observational study (Adams, 2007) lend further support to the presence of a cyclone at depth associated with the surface anticyclone. Cyclonic flow and negative pressure anomalies were associated with modeled anticyclonic eddies originating in the Gulf of Tehuantepec (Zamudio et al., 2006) and generically interacting with a slope (Hyun and Hogan, 2008). An episode of strong current velocities measured on the ridge axis (2500 m depth) was coincident with satellite observations of a large (>200 mm) positive sea level anomaly indicative of an anticyclonic Tehuantepec eddy. The observed near-bottom

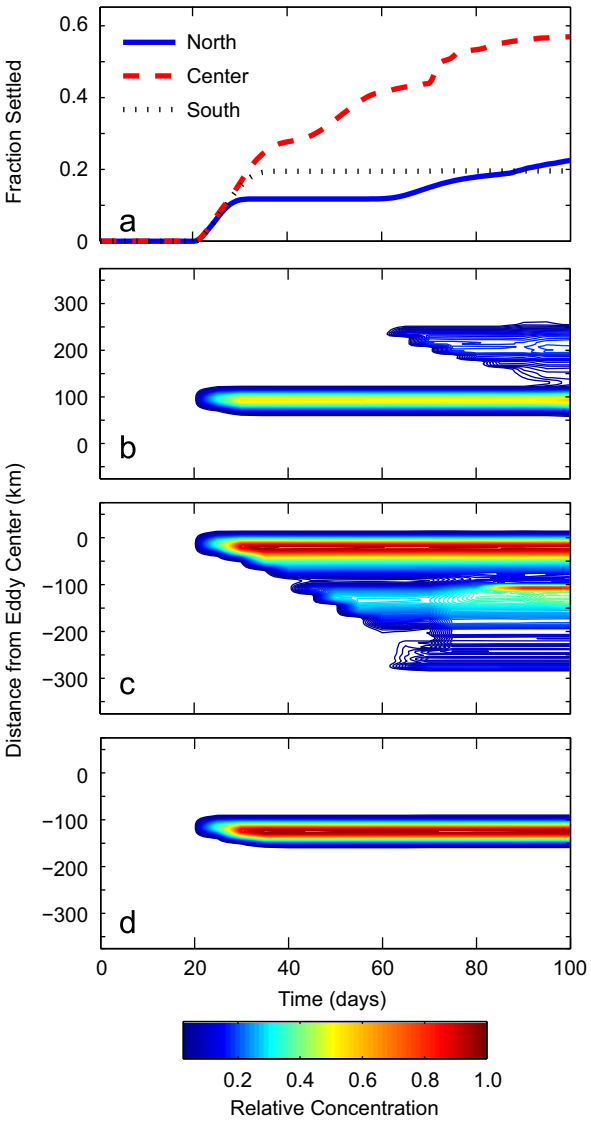

Fig. 9. (a) Cumulative percent of the total patch settled, for patches initiated 100 km north of the eddy center (blue, solid line), at the center of the eddy path (red, dashed line), and 100 km south of the eddy center (black, dotted line). Cumulative concentration of settlement along the ridge over 100 days for patches initiated (b) 100 km north of the eddy center, (c) at the center of the eddy path, and (d) 100 km south of the eddy center. The eddy was modeled using standard parameters with ridge topography. The contour interval is 0.01 and temporal resolution is 5 days for panels b–d. The origin is placed where the center of the eddy crosses the position of the ridge axis. (For interpretation of the references to colour in this figure legend, the reader is referred to the web version of this article.)

current velocities suggested the presence of a cyclonic eddy at depth (Adams, 2007). Both the models and observations were consistent with a vertical dipole with anticyclonic flow in the upper layer and a cyclonic flow in the lower layer. Thus, Tehuantepec eddies may form hetons (vertical dipoles) that are hypothesized to be important in the transport of heat (Hogg and Stommel, 1985), salinity and particles.

4.3. Ridge interactions strengthen transport between vents

Eddy-induced current velocities were sufficient to enhance deep-sea larval dispersal in general; however, the dispersal of vent larvae represents an unique case, in that suitable habitat is distributed only along the ridge. Thus not only does the distance of transport matter, but so does the direction. In the flat-bottom case, tracer could be transported 100s of kilometers, but very little, if any, of the tracer returned to the original longitudinal position. Assuming an approximately linear ridge axis with the tracer starting at the ridge, this would mean that little or no larvae would return to the ridge.

Simulated interactions of the deep cyclone with the ridge caused elongation and shearing which enhanced the potential for larval transport along the ridge (Figs. 7 and 8). The elongation and shearing increased meridional current velocities going up and down the ridge and increased transport back across the ridge. Interactions with the ridge also delayed propagation of the cyclone, increasing the residence time of the cyclone along the ridge topography. Thus, the hydrodynamic alterations induced by the ridge topography favored retention along the ridge axis, increasing the likelihood of successful larval transport among vents.

4.4. Ecological implications: re-colonization and connectivity

Episodic long-distance transport of larvae within eddies resolves the apparent contradiction between genetic and recent empirical estimates of dispersal along the East Pacific Rise. Genetic estimates suggest high levels of connectivity between populations separated by 100s of kilometers (e.g., Hurtado et al., 2004; Vrijenhoek et al., 1998). Similarly, the observed rapid recolonization of vents suggests a larval supply from distant sources (Mullineaux et al., 2010). However, recent observations of larval supply suggest that the bulk of the larvae supplied to established vents at 9°50′N originated from local sources (<5 km) (Adams and Mullineaux, 2008; Mullineaux et al., 2010). If self-recruitment is the dominant process, one might expect genetic drift and founder events to create genetic structure amongst the populations. Since only a few individuals need to be exchanged per generation to maintain high gene flow (Wright, 1931), episodic long-distance dispersal events are likely to dominate the genetic signal. The long-distance dispersal could then mask the primary contribution of local-larval supply. This is especially true for genetic markers with long temporal resolution. Similarly, only 10s of larvae may be required to colonize a nascent vent habitat. Simulated eddy-induced flows were sufficient to connect neighboring vent fields along the northern East Pacific Rise separated by up to 270 km (e.g. 11°N and 13°N). These episodic or stochastic long-distance dispersal events could account for the observed high genetic connectivity and rapid colonization, even with larval supply originating primarily from local sources at established vents.

Assuming that mesoscale eddies are a large contributor to long-distance dispersal, the simulated tracer experiments provide testable hypotheses about dispersal between the 13°N, 11°N, and 9°N vent fields. Since the success of settlement and transport depended on the latitude of the cyclone relative to the larval source, it is important to note that the majority of Tehuantepec eddies cross the ridge axis between 10°N and 14°N (Adams, 2007; Gonzalez-Silvera et al., 2004; Palacios and Bograd, 2005). The observed paths would place the center of the eddy across the 13°N and 11°N vent fields, and very rarely across the 9°N vent field. Based on the tracer transport along the ridge for an eddy with standard parameters (Figs. 7b and 9), larvae would be most likely transported southward between vent fields: from 11°N to 9°N (assuming the center is at 11°N) and from 13°N to 11°N (assuming the center is at 13°N). On the relatively rare occasion that the center crossed further south, larvae could be transported northward from 11°N to 13°N. Northward tracer transport from

the southern patch was observed for stronger eddies, which are relatively rare. Thus, we predict asymmetrical connectivity amongst these vent fields with higher southward exchange than northward exchange. In terms of metapopulation dynamics, we hypothesize that 11°N and 13°N act as sources, compared to 9°N which, relatively, acts as a sink.

Acknowledgments

We are grateful to Lauren Mullineaux, Susan Mills, Carly Strasser, Stace Beaulieu, Irene Garcia-Berdeal, Jesús Pineda, and Tim Shank for discussions at various stages of research and manuscript preparation. M.I.T.'s Project Athena provided computational resources. Comments from four anonymous reviewers improved the manuscript. Funding was provided by National Science Foundation Grant OCE-0424953 to L.S. Mullineaux and a National Defense Science and Engineering Graduate fellowship to D.K.A.

Appendix A. Model initialization

In order to verify the applicability of the quasi-geostrophic model to the Tehuantepec eddies, a series of experiments was performed to investigate the general vertical structure and propagation of the eddies.

A.1. Initialization of currents at depth

The dynamics of flow in the bottom layer were studied by varying the initial swirl speed in the lower layer, V_2. Simulations were initiated with anticyclonic flow ($V_2 < 0$), a still layer ($V_2 = 0$), and cyclonic flow ($V_2 > 0$) at depth. For an eddy with $l = 100$ km and $V_1 = -75\,\mathrm{cm\,s^{-1}}$, geostrophic cyclonic features developed in the lower layer independent of initial lower layer conditions. Initial current velocities for the lower layer were determined over a range of $V_2 = -20$ to $20\,\mathrm{cm\,s^{-1}}$, with no topography. Initial anticyclonic flow ($V_2 = -20$ to $-5\,\mathrm{cm\,s^{-1}}$) in the lower layer decayed through the rapid radiation of Rossby waves (Fig. A1). Rossby waves were seen quickly propagating westward, dissipating the anticyclonic vorticity. A cyclone formed in place of the anticyclone and strengthened as it propagated as a coherent feature (Fig. A1). An initial motionless lower layer ($V_2 = 0$) developed into paired vortices, with an anticyclone to the west and a cyclone to the east (data not shown). The anticyclone again radiated as Rossby waves, leaving a cyclonic eddy in the lower layer associated with the anticyclonic eddy in the surface layer. A weaker anticyclonic feature formed in the wake of the cyclonic eddy.

Since the development of the anticyclonic feature in the wake could have been due to the Rossby waves wrapping around the domain, V_2 was optimized to reduce the radiation of Rossby waves. Initial cyclonic flow of 15–20 $\mathrm{cm\,s^{-1}}$ reduced Rossby wave radiation to negligible levels. The anticyclonic feature still developed in the wake of the cyclone but more slowly. All subsequent simulations were performed with an initial cyclonic swirl speed $V_2 = 15\,\mathrm{cm\,s^{-1}}$ (a pure baroclinic mode), unless otherwise noted.

A.2. Propagation

Propagation speed and direction were investigated for the flat-bottom case for various l and V_1 to determine appropriate initialization parameters. As previously shown (McWilliams and Flierl, 1979), increasing the radius increased the direction of propagation and increased the propagation speed; and increasing the swirl speed resulted in decreased direction of propagation and increased propagation speed. Propagation speeds ranged from 11.2–16.2 $\mathrm{cm\,s^{-1}}$, within the range of observed propagation speeds of Tehuantepec eddies (Table 1). The direction of propagation varied between 246° and 254°, again within the range of observations for Tehuantepec eddies (Table 1).

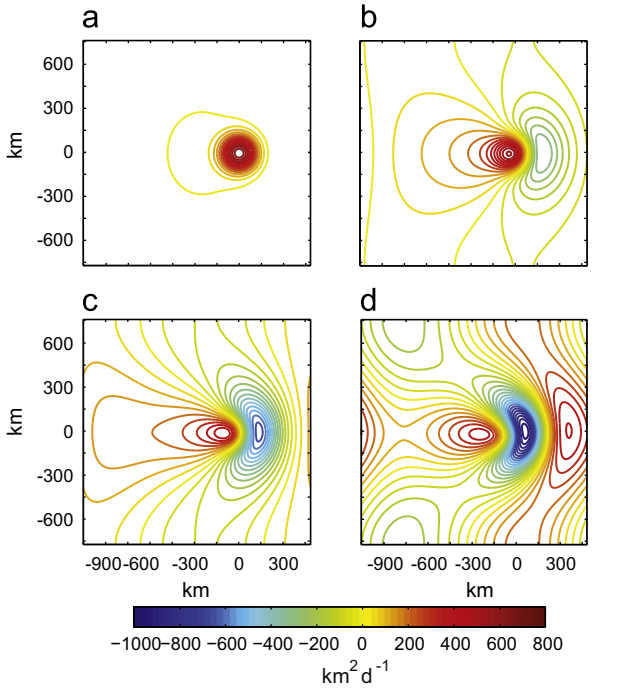

Fig. A1. Contours of the stream function in the lower layer $\psi_2(x,y,t)$ using standard upper layer parameters and an initial anticyclonic swirl of $V_2 = -5$ cm $\mathrm{s^{-1}}$ in the lower layer at (a) $t = 0.5$ d, (b) $t = 2.5$ d, (c) $t = 5$ d, and (d) $t = 10$ d. Note the rapid decay and propagation of the initial anticyclonic feature (positive ψ−warm colors) and the development and strengthening of a cyclonic feature (negative ψ−cool colors). The contour interval was $50\,\mathrm{km^2\,d^{-1}}$ for all plots. The origin is placed at the initial position of the eddy. (a) $t = 0.5$ d. (b) $t = 2.5$ d. (c) $t = 5.0$ d. (d) $t = 10$ d. (For interpretation of the references to colour in this figure legend, the reader is referred to the web version of this article.)

The upper and lower layers did not propagate as a cohesive unit. For an eddy with standard parameters, the upper layer propagated west–southwest (248°) at $11.5\,\mathrm{cm\,s^{-1}}$, while the lower layer initially propagated more slowly ($6.2\,\mathrm{cm\,s^{-1}}$) in the direction of 282°. After 25 days of propagation, there was a lag between the centers of the cyclone in the lower layer and the anticyclone in the upper layer (Fig. 2a). Despite the differences in trajectories, the spatial extent of the vortices in the upper and lower layers still overlapped. As the distance between the surface anticyclone and the lower cyclone increased, the propagation speed of the cyclone increased closing the zonal gap (Fig. 2b) and the trajectory of the cyclone became more westerly (as opposed to west–northwest) (Fig. 2c). The changes in speed and trajectory support the idea that the two vortices continued to interact throughout the experiment.

Appendix B. Ridge interactions

Modeled dipole eddies crossed the ridge topography with ease compared to previous modeling studies which found strong interactions between Agulhas-like eddies and a meridional ridge (Beismann et al., 1999; Sansón, 2002; van Geffen and Davies, 2000). Depending on the initial starting position and conditions,

these studies showed that the ridge destroyed, reflected, or trapped the eddies. In the present experiments, the surface anticyclone crossed the ridge with little deviation from its flat-bottom path (Fig. B1a). Using standard parameters, propagation speed decreased from 12.9 to 12.8 cm s^{-1} with the addition of topography, close to the limit of detection based on grid size. The direction of propagation changed from 249.4° over a flat bottom to 249.7° over the ridge (Fig. B1a), again close to the limit of detection based on grid size. Ridge topography had a larger effect on the surface swirl speed (Fig. B1b). When the eddy began interacting with the ridge ($t \simeq 35$ d), the maximum absolute swirl speed decreased. Once the center of the eddy crossed the ridge axis on day 50, the maximum absolute swirl speed increased again. While the cyclone in the lower layer deformed and weakened, it recovered and also crossed the ridge (Fig. 3).

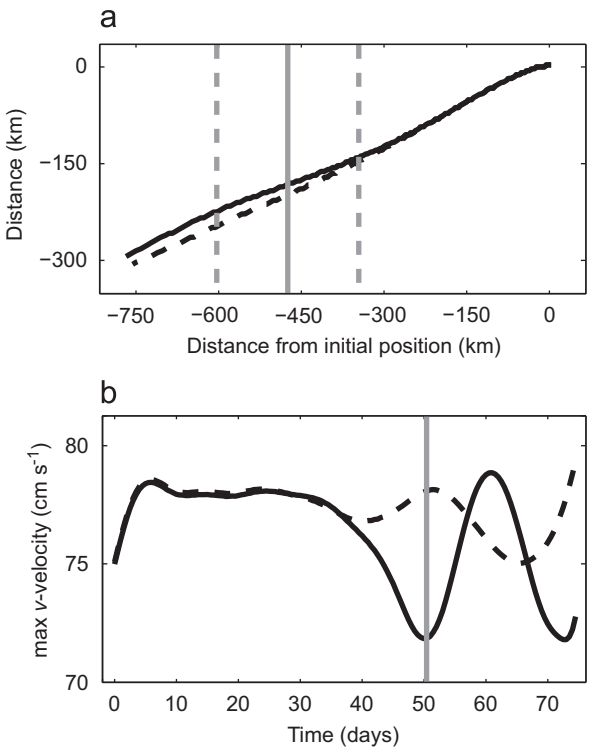

Fig. B1. (a) Trajectories of the spatial maximum of ψ_1 (upper layer) over 75 days for standard parameters with (solid line) and without (dashed line) ridge topography. Solid gray line denotes the ridge axis. Dashed gray lines denote the extent of the ridge topography. (b) Maximum meridional velocity, v_1, over time in the upper layer over 75 days for the standard parameters with (solid line) and without (dashed line) ridge topography. Solid gray line denotes approximate time when the center of the anticyclone was over the ridge axis.

The vertical structure may account for the differences between the present study and the Agulhas papers. The Agulhas studies considered barotropic vortices or monopoles with the flow at depth in phase with flow at the surface. If the flow in the lower layer decayed sufficiently through the radiation of Rossby waves (Beismann et al., 1999) or if baroclinic instabilities were included (Kamenkovich et al., 1996), the simulated eddies could cross the ridge topography. Linear theory, described in detail below, indicates that baroclinic waves are transmitted across the ridge much more readily than barotropic disturbances. Both modes contribute to the dynamics of the eddies considered here. The Burger number, $\mathrm{Bu} = (NH)^2/(fl)^2 = (R_D/l)^2$, where N is the buoyancy frequency, is order one, so that vorticity and vertical stretching contribute roughly equally to the potential vorticity structure for our standard eddy. The deep cyclone was partially decoupled from the surface eddy: the trajectories deviated from each other. In terms of modes, this implies that barotropic flows developed from the initially purely baroclinic vortex ($H_1\psi_1 = -H_2\psi_2$), both from the nonlinearity and from the interaction with topography (Fig. B2). Initially, the energy is all in the baroclinic mode, but the barotropic energy begins growing (e.g. McWilliams and Flierl, 1979) and the transfer continues as the barotropic waves radiate away (Flierl, 1984). But as the eddy moves over topography, the flow becomes more baroclinic again since the deep signal is partially blocked, disrupting the correlation between the stream functions in the two layers. After the eddy passes the ridge, it again begins to lose energy into barotropic waves. The shear and decoupling between the two layers accounts for the ability of these eddies to cross the ridge with little change in the surface eddy trajectory.

B.1. *Transmission of Rossby waves across a ridge*

We consider the transmission and reflection of Rossby waves with westward group velocity across a ridge $b(x)$ in the two layer model. The linearized equations

$$\frac{\partial q_1}{\partial t} + \beta \frac{\partial \psi_1}{\partial x} = 0, \quad \frac{\partial q_2}{\partial t} + \beta \frac{\partial \psi_2}{\partial x} - S(x) \frac{\partial \psi_2}{\partial y} = 0,$$

with $S = (f_0/H_2)\partial b/\partial x$ have solutions

$$\psi_i = \phi_i(x) \exp(\imath \ell y - \imath \omega t).$$

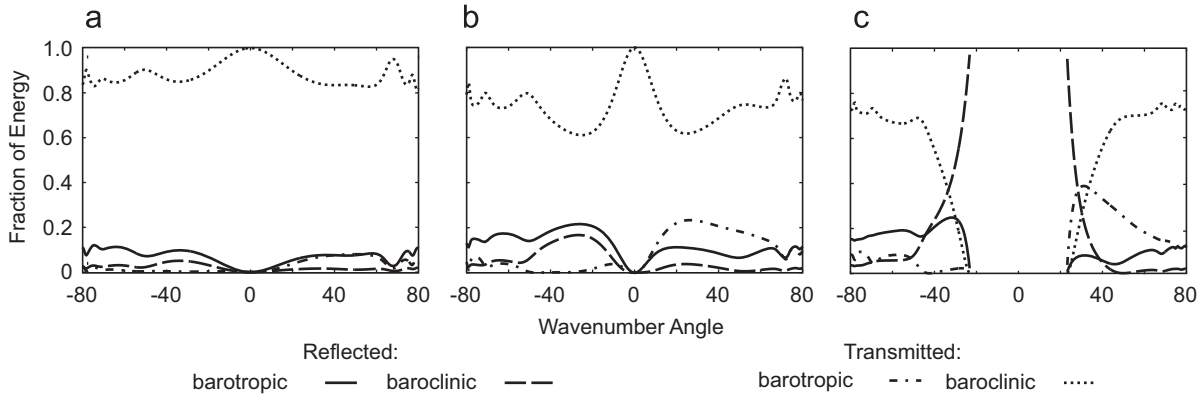

Fig. B2. Fraction of the reflected barotropic (solid line) and baroclinic (dashed line) energy fluxes and of the transmitted barotropic (dash-dot line) and baroclinic (dotted line) energy fluxes as a function of the angle (from east) of the incident wavenumber vector for wave scales of (a) 150 km, (b) 100 km, and (c) 75 km. The fluxes are the wave energy multiplied by the group velocity. $\mathbf{k} = [1/scale](\cos\theta, \sin\theta)$.

In that case the dynamical equations reduce to coupled second order ODE's for $\phi_i(x)$. (If we had included the mean flow the order would be raised and the solutions in the flat regions would be less simple; we have not studied that complication.) We can rewrite this systems as a set of first-order equations for

$$\Phi = \begin{bmatrix} \phi_1(x) \\ \frac{\partial}{\partial x}\phi_1(x) \\ \phi_2(x) \\ \frac{\partial}{\partial x}\phi_2(x) \end{bmatrix},$$

which can be stepped to the right (or left) by solving

$$\frac{\partial}{\partial x}\Phi = \begin{bmatrix} 0 & 1 & 0 & 0 \\ \ell^2+F_1 & -\imath\frac{\beta}{\omega} & -F_1 & 0 \\ 0 & 0 & 0 & 1 \\ -F_2 & 0 & \ell^2+F_2-S\frac{\ell}{\omega} & -\imath\frac{\beta}{\omega} \end{bmatrix} \Phi \equiv \mathbf{M}\Phi. \tag{B.1}$$

From this, we can define a 4×4 propagator matrix $\mathbf{P}(x_e, x_w)$ which relates the values of Φ on the east side of the ridge to those on the west

$$\Phi(x_e) = \mathbf{P}(x_e,x_w)\Phi(x_w).$$

To find $\mathbf{P}$, we start at x_w with Φ equal to an identity matrix and integrate (Eq. B.1) to x_e; the propagator (perhaps more accurately the reverse propagator, since the waves we consider will flux energy westward) is the resulting matrix.

For the transmission/reflection problem, we start with the facts that (1) the waves in the flat regions to the east and west can be decomposed in barotropic (subscript T) and baroclinic (C) modes and (2) the incident and transmitted waves will be the long waves with westward group velocity, while the reflected waves will be the short waves with eastward group velocity. For a given ω and ℓ, we can find two barotropic and two baroclinic wavenumbers k_T, k'_T, k_C, and k'_C which satisfy the dispersion relations $k_T^2+\ell^2+\beta k_T/\omega = 0$ and $k_C^2+\ell^2+F_1+F_2+\beta k_C/\omega = 0$ (although we may have complex wavenumbers, in which case, we chose the one which decays in the correct direction). We denote the larger solution with a prime; this is the shorter wave which will have eastward group velocity.

We can write $\Phi(x_e)$ in terms of the complex barotropic and baroclinic reflection coefficients R_T and R_C as

$$\Phi(x_e) = \begin{bmatrix} 1 \\ \imath k_i \\ a \\ a\imath k_i \end{bmatrix} + R_T \begin{bmatrix} 1 \\ \imath k'_T \\ 1 \\ \imath k'_T \end{bmatrix} + R_C \begin{bmatrix} 1 \\ \imath k'_C \\ -\delta \\ -\delta\imath k'_C \end{bmatrix} \equiv \Phi_I + R_T\Phi_{RT} + R_C\Phi_{RC}.$$

Here $\delta = H_1/H_2$, and $a=-\delta$, $k_i=k_C$ for a baroclinic incident wave or 1, k_T for a barotropic one. But we can also compute $\Phi(x_e)$ by propagating the barotropic plus baroclinic transmitted waves from x_w back to x_e

$$\Phi(x_e) = \mathbf{P}(x_e,x_w)\left(T_T \begin{bmatrix} 1 \\ \imath k_T \\ 1 \\ \imath k_T \end{bmatrix} + T_C \begin{bmatrix} 1 \\ \imath k_C \\ -\delta \\ -\delta\imath k_C \end{bmatrix} \right) \equiv T_T\Phi_{TT} + T_C\Phi_{TC}.$$

Equating these and rearranging leads to a matrix equation

$$\Phi_I = [-\Phi_{RT} \;\; -\Phi_{RC} \;\; \Phi_{TT} \;\; \Phi_{TC}] \begin{bmatrix} R_T \\ R_C \\ T_T \\ T_C \end{bmatrix}. \tag{B.2}$$

Recall that the Φ's are 4×1 column vectors, so the right hand side indeed has a 4×4 matrix multiplying a 4×1 vector of coefficients. Solving this linear system tells us the amplitude of the transmitted and reflected waves.

Previous studies have examined barotropic waves (e.g., Barnier, 1984; Matano, 1995; Rhines, 1969). Baroclinic studies include a knife-edge ridge (Owen et al., 2002) and a 'top-hat' profile (Wang and Koblinsky, 1994). In contrast, we have used piecewise-linear profiles, starting with a triangle, and ending with the complex topography used in the numerical experiments. We represented the ridge as 3 km line segments joining the data points; using the original 0.5 km data gave virtually identical results. For a linear slope, $\mathbf{M}$ in each subregion is constant; then the propagator in that section is just $\exp(\delta x\mathbf{M})$ [the matrix exponential]. $\mathbf{P}$ is the product of the propagators in each subregion. In Fig. B2, we show the transmission and reflection in terms of the ratio of the fluxes c_gE to the incident flux; as required, they total to one within machine accuracy. (Using a more conventional Runge–Kutta solver for Eq. (B.1) gives less accurate results.) We have partitioned the reflected and transmitted energies by mode. For long waves (Fig. B2a), most of the energy in the baroclinic wave passes over the ridge. When the scale L is 100 km, only slightly larger than the deformation radius (Fig. B2b), up to 40% of the energy can be reflected back when the waves are approaching from the northeast. Waves from due east do not feel the topography since their flows are purely meridional in the QG approximation; those coming from the southeast have about 30% of the energy transmitted as barotropic waves while 15% is reflected. For waves with scales shorter than the deformation radius (Fig. B2c), only those with high wavenumber angles will have westward group velocity; near the cutoff angle, the waves are completely reflected, but otherwise 70–80% of the energy is transmitted.

Barotropic waves will flux energy eastward unless $k<|\ell|$—the wavenumber angle is greater than 45°—but often a large fraction of it is reflected. For scales around 100 km, there is very little transformation into the baroclinic mode and that occurs at high angles.

Linear theory, therefore, suggests that the baroclinic signal of the eddy should be able to cross the ridge relatively easily, but the barotropic part will largely reflect or propagate away initially. The nonlinear simulations indeed show the upper layer eddy is relatively unaffected, while the deep flow is significantly altered. We have run the model with a nearly linear baroclinic eddy (without the large scale mean shear); the leading edge of the disturbance hits the topography fairly quickly and generates a

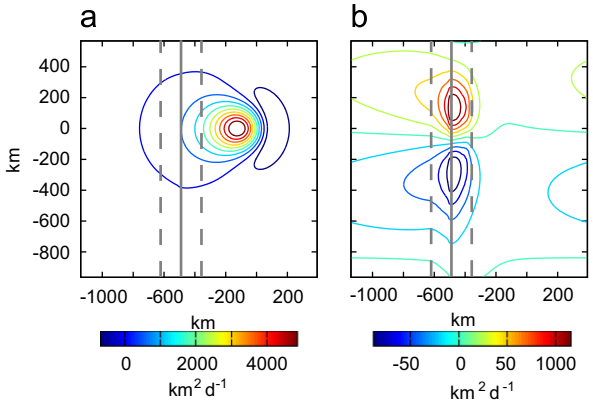

Fig. B3. (a) Baroclinic and (b) barotropic components of a standard eddy at 20 days. Note the generation of a barotropic dipole which rapidly radiates westward. The origin is placed at the initial position of the eddy. The solid gray line denotes the ridge axis. The dashed gray lines denote the extent of the topography.

barotropic dipole, creating waves propagating rapidly to the west (Fig. B3). We have not tried to make detailed comparisons since the eddy has a full spectrum of waves, the waves are not steady, and the model domain is doubly periodic. But the general character—the baroclinic signal mostly crossing the ridge, with the generation of barotropic waves—suggest that the calculations above give a reasonable picture of the interaction, even in the nonlinear regime.

References

Adams, D.K., 2007. Influence of hydrodynamics on the larval supply to hydrothermal vents on the East Pacific Rise. Ph.D. Thesis, Massachusetts Institute of Technology.

Adams, D.K., Mullineaux, L.S., 2008. Supply of gastropod larvae to hydrothermal vents reflects transport from local larval sources. Limnol. Oceanogr. 53, 1945–1955.

Backus, R.H., Flierl, G.R., Kester, D.R., Olson, D.B., Richardson, P.L., Vastano, A.C., Wiebe, P.H., Wormuth, J.H., 1981. Gulf Stream cold-core rings: their physics, chemistry, and biology. Science 212 (4499), 1091–1100.

Ballestero, D., Coen, J.E., 2004. Generation and propagation of anticyclonic rings in the Gulf of Papagayo. Int. J. Remote Sens. 25, 2217–2224.

Barnier, B., 1984. Energy transmission by barotropic Rossby waves across large-scale topography. J. Phys. Oceanogr. 14, 438–447.

Beismann, J.O., Käse, R.H., Lutjeharms, J.R.E., 1999. On the influence of submarine ridges on translation and stability of Agulhas rings. J. Geophys. Res. 104 (C4), 7897–7906.

Boehlert, G.W., Watson, W., Sun, L.C., 1992. Horizontal and vertical distributions of larval fishes around an isolated oceanic island in the tropical Pacific. Deep-Sea Res. 39, 439–466.

Canuto, C., Hussaini, M.Y., Quarteroni, A., Zang, T.A., 1988. Spectral Methods in Fluid Mechanics. Springer-Verlag.

Carbotte, S.M., Arko, R., Chayes, D.N., Haxby, W., Lehnert, K., O'Hara, S., Ryan, W.B.F., Weissel, R.A., Shipley, T., Gahagan, L., Johnson, K., Shank, T., 2004. New integrated data management system for Ridge2000 and MARGINS research. EOS Trans. AGU 85, 553. doi:10.1029/2004EO510002.

Chassignet, E.P., Cushman-Roisin, B., 1991. On the influence of a lower layer on the propagation of nonlinear oceanic eddies. J. Phys. Oceanogr. 21, 939–957.

Chelton, D.B., deSzoeke, R.A., Schlax, M.G., El Naggar, K., Siwertz, N., 1998. Geographical variability of the first baroclinic Rossby radius of deformation. J. Phys. Oceanogr. 28, 433–460.

Chevaldonné, P., Jollivet, D., Vangriesheim, A., Desbruyeres, D., 1997. Hydrothermal-vent alvinellid polychaete dispersal in the Eastern Pacific. 1. Influence of vent site distribution, bottom currents, and biological patterns. Limnol. Oceanogr. 42 (1), 67–80.

Clement, A.C., Gordon, A.L., 1995. The absolute velocity field structure of Agulhas eddies and the Benguela Current. J. Geophys. Res. 100 (C11), 22591–22601.

Cushman-Roisin, B., Chassignet, E.P., Tang, B., 1990. Westward motion of mesoscale eddies. J. Phys. Oceanogr. 20, 758–768.

de Ruijter, W.P.M., van Aken, H.M., Beier, E.J., Lutjeharms, J.R.E., Matano, R.P., Schouten, M.V., 2004. Eddies and dipoles around South Madagascar: formation, pathways and large-scale impact. Deep-Sea Res. I 51, 383–400.

Dewar, W.K., 1983. Atmospheric interactions with Gulf Stream rings. Ph.D. Thesis, Massachusetts Institute of Technology.

Doty, S., Oguri, M., 1965. The island mass effect. J. Conseil 22, 33–37.

Emery, A., 1972. Eddy formation from an oceanic island: ecological effects. Caribb. J. Sci. 12, 121–128.

Farrar, J.T., Weller, R.A., 2006. Intraseasonal variability near 10°N in the eastern tropical Pacific Ocean. J. Geophys. Res. 111, C05015 . doi:10.1029/2005JC002989.

Fiedler, P.C., Talley, L.D., 2006. Hydrography of the eastern tropical Pacific: a review. Prog. Oceanogr. 69, 143–180.

Flierl, G.R., 1984. Rossy wave radiation from a strongly nonlinear warm eddy. J. Phys. Oceanogr. 14, 47–58.

Flierl, G.R., 1987. Isolated eddy models in geophysics. Annu. Rev. Fluid Mech. 19, 493–530.

Flierl, G.R., 1994. Rings: semicoherent oceanic features. Chaos 4, 355–367.

Flierl, G.R., Stern, M.E., Whitehead, J.A., 1983. The physical significance of modons: laboratory experiments and general integral constraints. Dyn. Atmos. Oceans 7, 233–263.

Giese, B.S., Carton, J.A., Holl, L.J., 1994. Sea level variability in the eastern tropical Pacific as observed by TOPEX and Tropical Ocean–Global Atmosphere Tropical Atmosphere–Ocean Experiment. J. Geophys. Res. 99 (C12), 24,739–24,748.

Goni, G.J., Garzoli, S.L., Roubicek, A.J., Olson, D.B., Brown, O.B., 1997. Agulhas ring dynamics from TOPEX/POSEIDON satellite altimeter data. J. Mar. Res. 55, 861–883.

Gonzalez-Silvera, A., Santamaria-del Angel, E., Millán-Nuñez, R., Manzo-Monroy, H., 2004. Satellite observations of mesoscale eddies in the Gulfs of Tehuantepec and Papagayo (Eastern Tropical Pacific). Deep-Sea Res. II 51, 587–600.

Hansen, D.V., Maul, G.A., 1991. Anticyclonic current rings in the eastern tropical Pacific Ocean. J. Geophys. Res. 96 (C4), 6965–6979.

Heywood, K.J., Stevens, D.P., Bigg, G.R., 1996. Eddy formation behind the tropical island of Aldabra. Deep-Sea Res. I 43, 555–578.

Hogg, N.G., Stommel, H.M., 1985. The heton, an elementary interaction between discrete baroclinic geostrophic vortices, and its implications concerning eddy heat-flow. Proc. R. Soc. Lond. A 397, 1–20.

Hurtado, L.A., Lutz, R.A., Vrijenhoek, R.C., 2004. Distinct patterns of genetic differentiation among annelids of eastern Pacific hydrothermal vents. Mol. Ecol. 13 (9), 2603–2615.

Hyun, K.H., Hogan, P.J., 2008. Topographic effects on the anticyclonic vortex evolution: a modeling study. Cont. Shelf Res. 28 (10–11), 1246–1260.

Kamenkovich, V.M., Leonov, Y.P., Nechaev, D.A., Byrne, D.A., Gordon, A.L., 1996. On the influence of bottom topography on the Agulhas eddy. J. Phys. Oceanogr. 26, 892–912.

Kim, S.L., Mullineaux, L.S., Helfrich, K.R., 1994. Larval dispersal via entrainment into hydrothermal vent plumes. J. Geophys. Res. 99 (C6), 12655–12665.

Lee, T.N., Clarke, M.E., Williams, E., Szmant, A.F., Berger, T., 1994. Evolution of the Tortugas Gyre and its influence on recruitment in the Florida Keys. Bull. of Mar. Sci. 54, 621–646.

Marsh, A.G., Mullineaux, L.S., Young, C.M., Manahan, D.T., 2001. Larval dispersal potential of the tubeworm *Riftia pachyptila* at deep-sea hydrothermal vents. Nature 411, 77–80.

Matano, R.P., 1995. Numerical experiments on the effects of a meridional ridge on the transmission of energy by barotropic Rossby waves. J. Geophys. Res. 100 (C9), 18271–18280.

McCreary, J.P., Hyong, S.L., Enfield, D.B., 1989. The response of the coastal ocean to strong offshore winds: with application to circulations in the Gulfs of Tehuantepec and Papagayo. J. Mar. Res. 47, 81–109.

McWilliams, J.C., Flierl, G.R., 1979. On the evolution of isolated, nonlinear vortices. J. Phys. Oceanogr. 9, 1155–1182.

Müller-Karger, F., Fuentes-Yaco, C., 2000. Characteristics of wind-generated rings in the eastern tropical Pacific Ocean. J. Geophys. Res. 105 (C1), 1271–1284.

Mulhearn, P.J., Filloux, J.H., Lilley, F.E.M., Bindoff, N.L., Ferguson, I.J., 1986. Abyssal currents during the formation and passage of a warm-core ring in the East Australian Current. Deep-Sea Res. 33, 1563–1576.

Mullineaux, L.S., Adams, D.K., Mills, S.M., Beaulieu, S.E., 2010. Larvae from afar colonize deep-sea hydrothermal vents after a catastrophic eruption. Proc. Natl. Acad. Sci. USA 107, 7829–7834. doi:10.1073/pnas.0913187107.

Mullineaux, L.S., Mills, S.W., Sweetman, A.K., Beaudreau, A.H., Metaxas, A., Hunt, H.L., 2005. Vertical, lateral and temporal structure in larval distributions at hydrothermal vents. Mar. Ecol. Prog. Ser. 293, 1–16.

Nakata, H., Kimura, S., Okazaki, Y., Kasai, A., 2000. Implications of meso-scale eddies caused by frontal disturbances of the Kuroshio Current for anchovy recruitment. ICES J. Mar. Sci. 57 (1), 143–151.

Nof, D., 1981. On the β—induced movement of isolated baroclinic eddies. J. Phys. Oceanogr. 11, 1662–1672.

Owen, G.W., Abrahams, I.D., Willmott, A.J., Hughes, C.W., 2002. On the scattering of baroclinic Rossby waves by a ridge in a continuously stratified ocean. J. Fluid Mech. 465, 131–155.

Palacios, D.M., Bograd, S.J., 2005. A census of Tehuantepec and Papagayo eddies in the northeastern tropical Pacific. Geophys. Res. Lett. 32, L23606. doi:10.1029/2005GL024324.

Pedlosky, J., 1996. Ocean Circulation Theory. Springer, New York.

Rhines, P.B., 1969. Slow oscillations in an ocean of varying depth. Part 1. Abrupt topography. J. Fluid Mech. 37, 161–189.

Richardson, P.L., Fratantoni, D.M., 1999. Float trajectories in the deep western boundary current and deep equatorial jets of the tropical Atlantic. Deep-Sea Res. II 46, 305–333.

Sale, P.F., 1970. Distribution of larval Acanthuridae off Hawaii. Copeia, pp. 765–766.

Sangrá, P., Pelegrí, J.L., Hernández-Guerra, A., Arregui, I., Martín, J.M., Marrero-Díaz, A., Martínez, A., Ratsimandresy, A.W., Rodríguez-Santana, A., 2005. Life history of an anticyclonic eddy. J. Geophys. Res. 110, C03021. doi:10.1029/2004JC002526.

Sansón, L.Z., 2002. Vortex-ridge interaction in a rotating fluid. Dyn. Atmos. Oceans 35, 299–325.

Schonten, M.W., de Ruijter, W.P.M., van Leeuwen, P.J., Lutjeharms, J.R.E., 2000. Translation, decay and splitting of Agulhas rings in the southeastern Atlantic Ocean. J. Geophys. Res. 105 (C9), 21913–21925.

Sponaugle, S., Lee, T., Kourafalou, V., Pinkard, D., 2005. Florida Current frontal eddies and the settlement of coral reef fishes. Limnol. Oceanogr. 50 (4), 1033–1048.

Tracey, K.L., Watts, D.R., Meinen, C.S., Luther, D.S., 2006. Synoptic maps of temperature and velocity within the Subantarctic Front south of Australia. J. Geophys. Res. 111, C10016. doi:10.1029/2005JC002905.

van Aken, H.M., van Veldhoven, A.K., Veth, C., de Ruijter, W.P.M., van Leeuwen, P.J., Drijfhout, S.S., Whittle, C.P., Rouault, M., 2003. Observations of a young Agulhas ring, Astrid, during MARE in March 2000. Deep-Sea Res. II 50, 167–195.

van Geffen, J., Davies, P., 2000. A monopolar vortex encounters a north–south ridge or trough. Fluid Dyn. Res. 26, 157–179.

Vrijenhoek, R.C., Shank, T., Lutz, R.A., 1998. Gene flow and dispersal in deep-sea hydrothermal vent animals. Cah. Biol. Mar. 39, 363–366.

Wang, L., Koblinsky, C., 1994. Influence of mid-ocean ridges on Rossby waves. J. Geophys. Res. 99 (C12), 25143–25153.

Willett, C.S., Leben, R.R., Lavín, M.F., 2006. Eddies and tropical instability waves in the eastern tropical Pacific: a review. Prog. Oceanogr. 69, 218–238.

Wright, S., 1931. Evolution in mendelian populations. Genetics 16, 97–159.

Zamudio, L., Hurlburt, H.E., Metzger, E.J., Morey, S.L., O'Brien, J.J., Tilburgh, C., Zavala-Hidalgo, J., 2006. Interannual variability of Tehuantepec eddies. J. Geophys. Res. 111, C05001. doi:10.1029/2005JC003182.